Cell & Bioscience

RESEARCH

Open Access

The interwoven fibril-like structure of amyloid-beta plaques in mouse brain tissue visualized using super-resolution STED microscopy

Björn Johansson[1,2], Sho Oasa[1], Aida Muntsant Soria[3,4], Ann Tiiman[1], Linda Söderberg[5], Ebba Amandius[5], Christer Möller[5], Lars Lannfelt[5], Lars Terenius[1], Lydia Giménez-Llort[3,4] and Vladana Vukojević[1*]

Abstract

Background Standard neuropathologic analysis of Alzheimer's brain relies on traditional fluorescence microscopy, which suffers from limited spatial resolution due to light diffraction. As a result, it fails to reveal intricate details of amyloid plaques. While electron microscopy (EM) offers higher resolution, its extensive sample preparation, involving fixation, dehydration, embedding, and sectioning, can introduce artifacts and distortions in the complex brain tissue. Moreover, EM lacks molecular specificity and has limited field of view and imaging depth.

Results In our study, we employed super-resolution Stimulated Emission Depletion (STED) microscopy in conjunction with the anti-human APP recombinant antibody 1C3 fluorescently labelled with DyLight^{TM}633 (1C3-DyLight633). This combination allowed us to visualize amyloidogenic aggregates in vitro and in brain sections from a 17-month-old 3×Tg-AD mouse with sub-diffraction limited spatial resolution. Remarkably, we achieved a spatial resolution of 29 nm in vitro and 62 nm in brain tissue sections, surpassing the capabilities of conventional confocal microscopy by 5–10 times. Consequently, we could discern individual fibrils within plaques, an achievement previously only possible with EM.

Conclusions The utilization of STED microscopy represents a groundbreaking advancement in the field, enabling researchers to delve into the characterization of local mechanisms that underlie Amyloid (Aβ) deposition into plaques and their subsequent clearance. This unprecedented level of detail is especially crucial for comprehending the etiology of Alzheimer's disease and developing the next generation of anti-amyloid treatments. By facilitating the evaluation of drug candidates and non-pharmacological interventions aiming to reduce amyloid burden, STED microscopy emerges as an indispensable tool for driving scientific progress in Alzheimer's research.

Keywords Alzheimer's disease, Amyloid beta peptide, Amyloid fibrils, Immunohistochemistry, Super-resolution STED microscopy, Next generation drug design

*Correspondence:
Vladana Vukojević
vladana.vukojevic@ki.se
Full list of author information is available at the end of the article

Introduction

The major component of plaques found in the brains of patients with Alzheimer´s disease (AD) are 40–42 amino acids long amyloid beta (Aβ) peptides derived from the amyloid precursor protein (APP) by enzymatic cleavage, first with β-secretase (BACE1) and then by γ-secretase [1, 2]. Immunohistochemistry has significantly contributed to mapping the distribution of Aβ peptides and Aβ amyloidogenic fibrils in the brain, both at the inter- and intracellular level. For example, $A\beta_{42}$ was found in the nuclear envelope and endoplasmic reticulum, whereas $A\beta_{40}$ was found to be restricted to the trans-Golgi network [3]. It was early on observed that the intracellular pathology becomes less evident as the extracellular Aβ deposition progresses, which has led D'Andrea to propose that intracellular Aβ can contribute to the generation of amyloid plaques in the human brain [4]. More precisely, using antibodies against $A\beta_{40}$ and $A\beta_{42}$, it was found that $A\beta_{42}$ accumulated in granular bodies inside pyramidal neurons of AD brains [5]. Based on observations of an inverse relationship between plaque density and pyramidal neuron density, chromatin abnormalities in pyramidal neurons rich in $A\beta_{42}$, larger intracellular $A\beta_{42}$ granules in areas with higher plaque density and nuclear remnants in the dense core of plaques, it was suggested that $A\beta_{42}$ amyloid fibrils first accumulate inside the neurons which eventually die, releasing their amyloid content from which the extracellular plaques are being formed in due course [4]. This notion of an intracellular pathology preceding extracellular plaque deposition was also supported by an independent immunocytochemical study by Gouras et al. [6] showing an age-dependent accumulation of intraneuronal $A\beta_{42}$ in non-AD subjects, especially in AD-vulnerable brain regions.

Electron microscopy (EM) has often been used to examine the structure and morphology of Aβ aggregates and aggregates composed of other amyloidogenic peptides. Aggregates originating from ex vivo materials and from synthetic peptides/proteins in vitro, have appeared to be similarly elongated (thread-like), unbranching, and of a comparable diameter (6–10 nm) [7], often consisting of filaments wound around one another [8]. However, using light microscopy, which has limited spatial resolution of 220 nm at best, the pathological Aβ-deposits observed in the brain tissue could only be described in collective terms, e.g. as amorphous, dense core or diffuse plaques [9–11], without much relation to the individual Aβ fibres seen with EM that were shown to develop protease resistance [12].

To specifically visualize the fibril network structure of Aβ amyloid plaques in brain tissue with improved spatial resolution, we have resorted to Stimulated Emission Depletion (STED) microscopy. STED microscopy was first experimentally realized at the turn of the millennium by the group of S.W. Hell [13], as the first optical super-resolution technology allowing imaging with a spatial resolution that goes beyond the barrier imposed by the diffraction of light. STED images are constructed by scanning across the sample two concentric lasers, a focused excitation laser beam that is of the highest intensity at the centre and the so-called STED laser beam that is of a longer wavelength and has lowest intensity at its centre and highest at its circumference. The STED laser forces the excited molecules that are localized outside its centre to lose energy through stimulated emission and return to the ground state before being able to emit fluorescence. In this way, spatial resolution down to tens of nanometers was achieved in live cells when small molecular probes such as silicon-rhodamine (SiR) or germano-rhodamine (GeR), aptamers (≈ 15 kDa; ≈ 4 nm) or nanobodies (≈ 13 kDa; ≈ 2–4 nm) are being used [14]. For immunostaining, the spatial resolution is somewhat lower due to antibody size (≈ 150 kDa; 10–15 nm) and even lower when a combination of a primary and a fluorescently labelled secondary antibody is being used – here the labelling complex becomes ≈ 30 nm and the probes often cannot bind to every target molecule due to spatial constraints, giving rise to "spotty" images and a spatial resolution that is ≈ 40 nm at best [14].

Thus far, STED microscopy has only been used in a handful of AD-related studies, e.g., to visualize amyloid fibrils in vitro [15]; characterize in the cerebrospinal fluid (CSF) of individuals with AD the number and size of Aβ and tau aggregates [16]; determine the localization of γ-secretase in the neuronal synapse in mouse hippocampal neurons in culture [17–19]; examine nanoscale features of spine morphology in the APP/PS1 mouse model of AD amyloidosis [20]; and visualize normal, unaggregated tau protein in the mouse brain [21]. Querol-Vilaseca et al. [22] used super-resolution in three dimensions by Array Tomography (AT) and STED microscopy, to characterize non-fibrillar Aβ structures in amyloid plaques in post-mortem human brain tissue of AD, revealing that an amyloid plaque is formed by a dense core of higher order Aβ species (22 nm^3) and a peripheral halo of smaller Aβ structures (3 nm^3); whereas Hernández et al. combined STED with selective plane illumination microscopy (STED-SPIM) to image AD-related brain pathology with improved optical slicing [23]. In relation to other amyloid diseases, STED microscopy of cellular uptake of α-synuclein oligomers, putative causative agents in Parkinson's disease, was recently described [24] and STED imaging of a Thioflavin T labelled amyloid of an α-synuclein mutant was developed [25]; STED was

used to characterize huntingtin aggregates and sequestration in inclusion bodies [26], and to visualize apoferritin amyloid fibrils formation [27].

Recent success in the development of immunotherapies against Aβ for the treatment of AD [28] have renewed the interest in characterising the affinity profile and binding kinetics of monoclonal antibody drug candidates [29, 30], and have also highlighted the need for characterizing local mechanisms through which plaque formation/clearance is achieved. In this study, we show that STED microscopy allows us to visualize individual fibrils in plaques in brain tissue sections at a spatial resolution that is 5–10 times better than using conventional confocal microscopy.

Materials and methods

Animals and brain sections

Experiments were performed in accordance with the relevant guidelines from the Swedish National Board for Laboratory Animals, the Spanish legislation and the European Community Council Directive (2010/63/UE) on this subject under the protocol CEEAH 3588/DMAH 9452. The present study includes the analysis of brain sections from one 17-month-old 3×Tg-AD mouse bearing three human mutant genes: presenilin-1 (PS1) with the M146V mutation, the human APP gene with the Swedish mutation, and tau with the P301L mutation [31]. Mice were kept under standard laboratory conditions at Universitat Autònoma de Barcelona, with food and water ad libitum, T = (22 ± 2) °C, under a 12:12 h light: dark cycle and relative humidity of 40–60%. Euthanasia was performed using CO_2. The brains were quickly dissected and immediately frozen on dry ice, followed by storage at −80 °C. Sagittal sections of 16 µm thickness were cut using a cryostat (Leica Jung CM 3000, Leica Microsystems, Wetzlar, Germany) at approximately −20 °C. Sections were collected on Superfrost Plus glass slides (Gerhard Menzel GmbH, Braunschweig, Germany) and stored at −20 °C. Sections cut at 2.88–2.90 mm from brain's midline were selected and processed for immunohistochemistry as described below.

Antibodies

Monoclonal anti-human APP recombinant antibody 1C3 that detects the linear N-terminal fragment comprising residues 2–8 and is not conformation specific [32] fluorescently labelled with DyLight™ 633.

Immunohistochemistry

For immunohistochemistry, brain tissue sections were blocked for 30 min with 10% horse serum, 5 mg/ml bovine serum albumin and 0.2% Triton X-100 in PBS. For amyloid plaque visualization, AD brain tissue sections were immunostained for 1 h using 500 nM 1C3-DyLight633 (BioArctic, Stockholm, Sweden). In immunohistochemistry control experiments, 1C3-DyLight633 binding was blocked by simultaneous co-incubation with unlabelled $A\beta_{40}$ in large excess, 100 µg/ml (23 µM). For nuclear staining, the ProLong™ Gold Antifade Mountant with DAPI (ThermoFisher, P36935) was used following manufacturer's instructions.

$A\beta_{40}$ aggregation in vitro

50 µg of the human recombinant $A\beta_{40}$ peptide (Alexo-Tech AB, Umeå, Sweden) was dissolved in 50 µl of 10 mM NaOH and incubated at room temperature for 1 min. The peptide/NaOH solution was diluted to 10 µM peptide concentration with 20 mM HEPES buffer (pH 7.4) and incubated at room temperature for 1 h while stirring at 1100 rpm. After turning off the stirrer, the sample was allowed to rest and a 5 µl aliquot of $A\beta_{40}$ aggregates that accumulated at the bottom of the reaction vessel was pipetted out and transferred to the grid for EM imaging. For STED microscopy, a 100 µl aliquot of $A\beta_{40}$ aggregates that accumulated at the bottom of the reaction vessel was pipetted out, mixed with 1C3-DyLight633 to a 1C3-DyLight633 concentration of 500 nM, transferred to a #1.5 coverglass (VWR, 631 − 0136) and imaged. The $A\beta_{40}$ aggregates were always freshly prepared before imaging.

Transmission Electron Microscopy (TEM) imaging

A formvar coated TEM grid stabilized with evaporated carbon film on 200 mesh copper (Formvar/Carbon Film coated, 200 Mesh, Cu) was first hydrophilized by treatment in an EMS 100× glow discharge unit for 45 s at the current of 25 mA. Thereafter, a 5 µl aliquot of freshly prepared $A\beta_{40}$ aggregates was transferred to the grid and incubated for 1 min at room temperature. The droplet was removed with a pipette and the specimen was negatively stained following the procedure described by Keller et al. [33]. Briefly, a 5 µl droplet of freshly prepared 1% uranyl acetate (UAc) was applied to the grid and incubated for a few seconds. The UAc droplet was removed and a fresh 5 µl UAc droplet was applied. The application-removal cycle was repeated seven times. Following the removal of the last droplet, the sample was air-dried for several minutes and subjected to TEM imaging using a Talos L120C transmission electron microscope (Thermo Fisher Scientific) operating at 120 kV. The images were acquired using a Ceta-D camera.

Confocal laser scanning Microscopy (CLSM) imaging of whole brain tissue sections

CLSM imaging was performed using an LSM880 (Carl Zeiss) microscope system equipped with a

633 nm He-Ne laser, objective lens (Plan-Apochromat 10×/N.A. 0.45 M27), and a 32-channel gallium arsenide phosphide (GaAsP) spectral detector. DyLight^{TM}633 fluorescence was excited using the 633 nm HeNe laser. The pinhole size was 90 µm. Fluorescence was spectrally split by gratings and detected in the 638–755 nm range by the GaAsP detector. The tile scan function was used to acquire an image series of neighboring fields of view and construct images of the whole mouse brain tissue section (size: 9 mm × 7 mm).

Stimulated Emission Depletion (STED) microscopy imaging

Super-resolution STED and related CLSM images were acquired at the same position using the STEDYCON compact line nanoscope (Abberior Instruments GmbH, Göttingen, Germany) mounted on an Zeiss Axio Imager Z2 (Carl Zeiss) microscope. The STEDYCON nanoscope unit is equipped with a 405 nm continuous wavelength laser, a 640 nm pulsed excitation laser and a 775 nm pulsed STED laser; oil immersion objective (Plan-Apochromat 100×/N.A. 1.46 Oil DIC M27) and avalanche diode detectors (APDs). DAPI and DyLight633 fluorescence were excited using the 405 nm and the 640 nm lasers, respectively. The pinhole size was 64 µm. The fluorescence was split and detected by distinct APDs (DAPI: 420–475 nm, DyLight633: 650–700 nm). The STED laser power was set to 98% (maximum power) to acquire images with the highest spatial resolution possible.

Results

Super-resolution STED imaging of in vitro formed $A\beta_{40}$ aggregates

A STED image of $A\beta_{40}$ aggregates formed in vitro and immune-stained using the antibody 1C3-DyLight633 (Fig. 1A), showed spatially well-resolved fibrils (Fig. 1A and B) that could not be easily discerned in the diffraction-limited image acquired by conventional confocal microscopy (Fig. 1C). TEM imaging (Fig. 1D), confirmed the STED microscopy findings, convincingly showing that most of the precipitated aggregates are either single-thread filaments or twisted two-thread filaments (Fig. 1D). The smallest filament thickness, 29 nm, and average fibril thickness, (44 ± 13) nm, were discernable by STED microscopy, as evident from the full width at half-maximum (FWHM) of the fluorescence intensity distribution across the fibril (Fig. 1B). Given the antibody size (10–15 nm) and the thickness of the filament/fibril (7–14 nm), this value is in good agreement with the true size of the fibril–antibody complex.

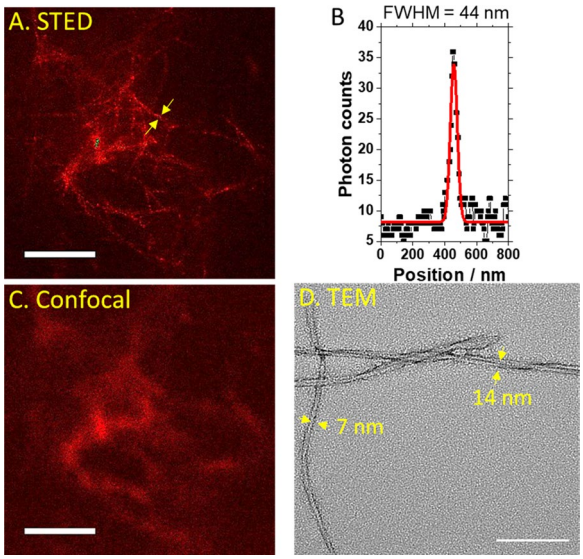

Fig. 1 Super-resolution STED microscopy and TEM images of in vitro formed $A\beta_{40}$ aggregates. **A** Super-resolution STED microscopy image of in vitro formed $A\beta_{40}$ aggregates rendered visible using 1C3-DyLight633. Scale bar 2 µm. **B** Fluorescence intensity profile along the fibril highlighted by yellow arrows showing a fibril diameter of 44 nm. **C** The diffraction-limited CLSM image of $A\beta_{40}$ aggregates shown in A. Scale bar 2 µm. **D** Negatively stained TEM image of in vitro formed $A\beta_{40}$ aggregates showing single-threaded filaments (7 ± 2) nm and twisted two-filament fibers (14 ± 1) nm. Scale bar 100 nm

Super-resolution STED imaging of Aβ aggregates in brain tissue sections

Whole mouse brain tissue sections (Fig. 2A) showed distinct regions of Aβ aggregates' accumulation (Fig. 2B) that were not observed in the negative control experiments, where antibody binding was blocked using a large excess (45–50 higher amount) of unlabelled $A\beta_{40}$ peptide (Fig. 2C). The photon count level in the negative control (Fig. 2C) was similar in intensity to the level measured in the brain regions devoid of Aβ aggregate deposits, PC ≈ 7 photons. These results indicate that the 1C3 antibody against Aβ specifically recognizes Aβ aggregates in the mouse brain tissue, without giving rise to an increased background due to unspecific binding. This further implies that the fluorescence signal above the background level, which was observed around the clearly discerned fibrils in the Aβ plaque, is due to monomeric Aβ and possibly also small-sized Aβ oligomers that could not be discerned by STED microscopy.

For further imaging with STED microscopy, we selected three brain regions where plaques were observed (Fig. 2B, yellow rectangles). The super-resolution STED images (Fig. $3A_{1\text{-}3}$, with corresponding CLSM images shown in Fig. $3B_{1\text{-}3}$), reveal that the smallest and the average fibril thickness determined by STED were 62 nm

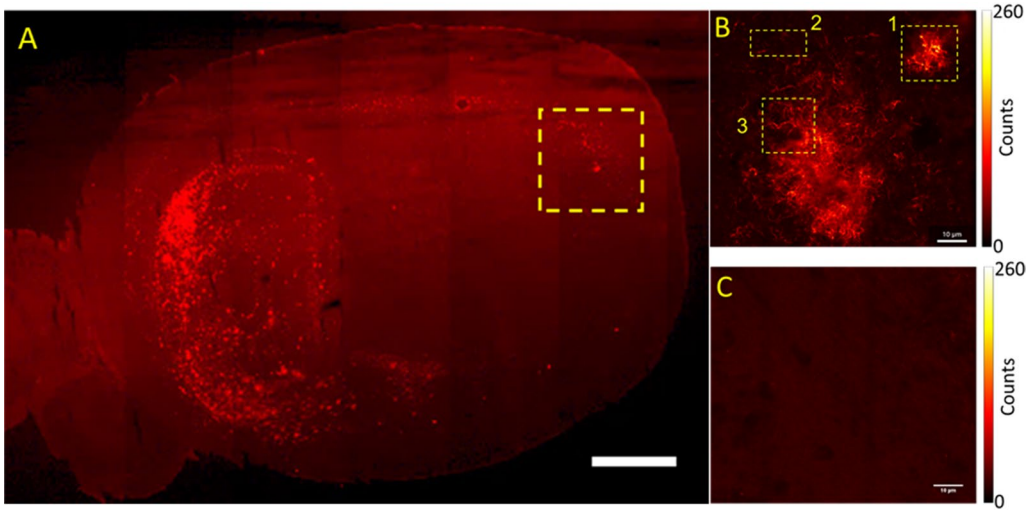

Fig. 2 CLSM images of Aβ amyloidogenic aggregates in a brain tissue section from a 17 months old 3×TgAD mouse. **A** Large-capture tile & stich CLSM image of a sagittal mouse brain section showing Aβ amyloid aggregates in the hippocampus (left) and the cerebral cortex (right), visualized using 1C3-DyLight633. Scale bar 2 mm. **B** Magnified CLSM image of the rectangular area highlighted in A. Different regions selected for super-resolution STED microscopy imaging (shown in Fig. 3) indicate: a small plaque (1), plaque outskirt (2) and a detail of a large plaque (3). Scale bar 10 µm. **C** Immunohistochemical control obtained by displacing 1C3-DyLight633 by simultaneous incubation with unlabelled $A\beta_{40}$ in large excess, (roughly 45 or 50 × higher). The average photon count in the background shown in C, $PC_{bg} \approx 7$ photons, is the same as the background in B, indicating that: (1) nonspecific binding of 1C3-DyLight633 is low and (2) regions characterized by fluorescence > PC_{bg} indicate the presence of Aβ monomers/small-sized oligomers that could not be resolved by STED imaging. Scale bar 10 µm

and (86 ± 18) nm, respectively (Fig. $3C_1$), compared to (320 ± 80) nm by CLSM. The STED images also showed that it was possible to successfully resolve two Aβ fibrils within a close distance, $d = 260$ nm, from one another (Fig. $3C_2$). Finally, dual-colour imaging with DAPI and 1C3-DyLight633 (Fig. $3A_3$ and B_3), compellingly showed that STED microscopy can resolve individual Aβ amyloid fibrils in cell-dense regions neighbouring the plaque, as well as within the plaque.

Discussion

This paper introduces super-resolution STED imaging of immunostained amyloid deposits in vitro (Fig. 1) and in brain tissue sections from an animal AD model (Fig. 3). STED microscopy enabled us to resolve details of the plaque structure that could not be resolved by confocal microscopy. Most notably, we were able to discern individual fibrils laying on top of one another in an untidy pile (Fig. 1A) that appeared by confocal imaging as a blurred diffuse smear (Fig. 1C) and measure their size—the average diameter of the in vitro formed fibrils was about (44 ± 13) nm in vitro, with the smallest diameter measured being 29 nm and the largest one 68 nm. The amyloid structures in brain tissue sections resolved in the present study are elongated, unbranched fibrils of an average fibril thickness of (86 ± 18) nm, ranging from 62 to 120 nm (Fig. 3), matching those in a recent in vitro STED study of an α-synuclein mutant with a 63-residue truncation in the N-terminal region that reported fine structures not resolved in confocal microscopy at a spatial resolution of 60–70 nm [25].

Based on the obtained results, several important STED microscopy applications are envisaged that could improve AD diagnostics and our understanding of basic mechanisms underlying AD.

Most notably, by pushing the boundaries of spatial resolution, Aβ tissue pathology can be examined at the nanoscale without resorting to EM. While indispensable in biomedical research—EM has been used to visualize with supreme spatial resolution details of synthetic amyloids structure in vitro, revealing the spacing between β-strands in a pleated β-sheet at a distance of 0.47 nm, protofilaments diameter of 3 nm, and fibrils of 8–10 nm in diameter (reviewed in [8]); has shown that different peptides/proteins, irrespective of their primary structure, chain length and native conformation, can acquire a prototypical, fibrillar amyloid structure [34–36]; and that amyloid filaments (dispersed to be suitable for cryo-EM reconstruction) may show AD-specific differences in interprotofilament packing [37], diagnostic EM is not widely available. The possibility to visualize Aβ tissue pathology at the nanoscale spatial resolution using STED microscopy is of relevance as the local environment in which peptides/proteins assemble into amyloid fibrils may significantly affect their morphology, giving rise to variations in twist periodicity, number of bundled

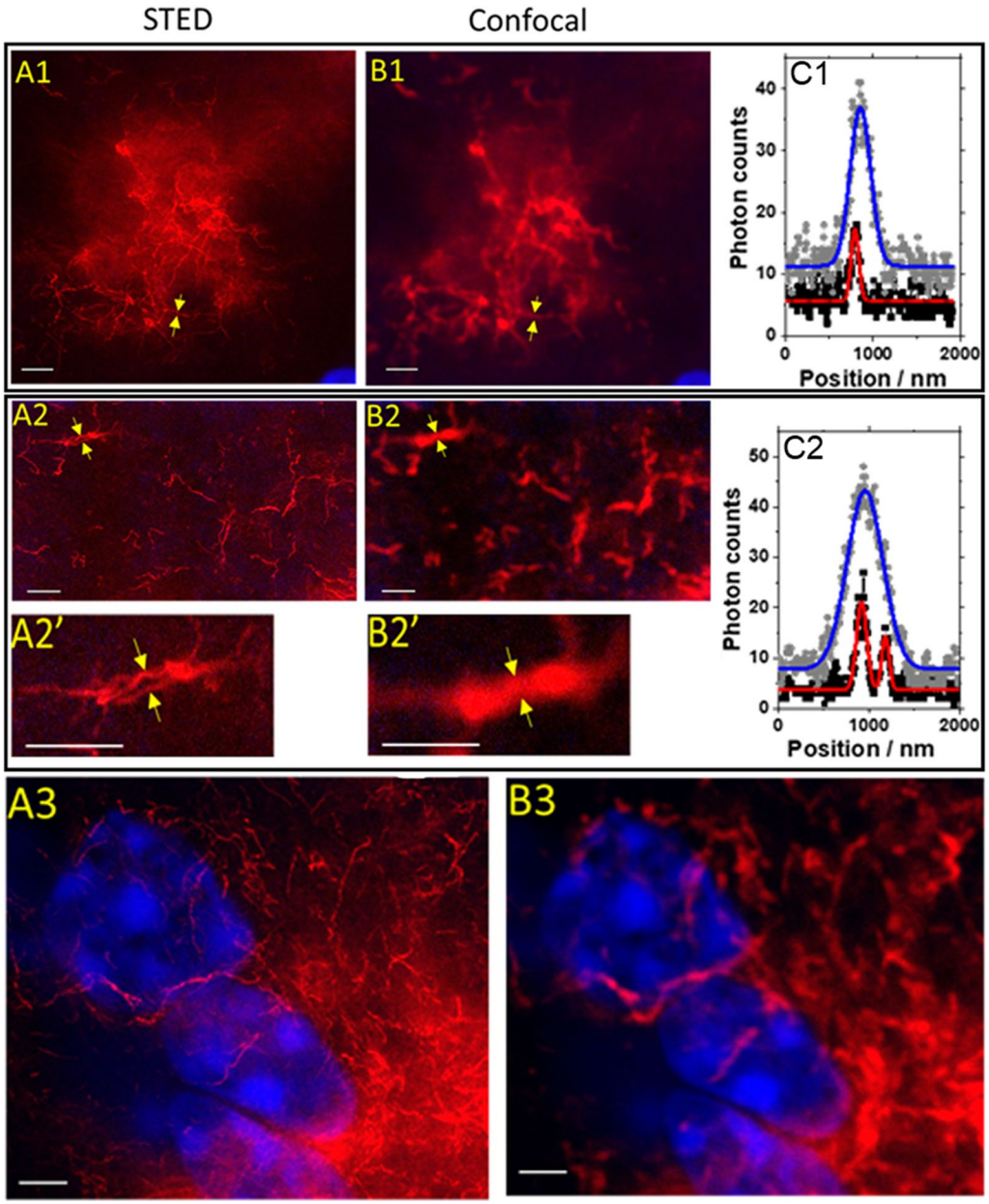

Fig. 3 STED and CLSM images of Aβ amyloid aggregates in a brain tissue section from a 17 months old 3×TgAD mouse. **A1/B1** STED (**A1**) and CLSM (**B1**) images of a small plaque. The yellow arrows point to a detail at the plaque outskirt. **C1** Fluorescence intensity distribution profile shows that the detail from **A1**/**B1** is a single fiber with an apparent diameter of 87 nm measured by STED (black squares and corresponding Gaussian fit (red line)) and 320 nm by Confocal (grey diamonds and corresponding Gaussian fit (blue line)). **A2/B2** STED (**A2**) and CLSM (**B2**) images of a detail in the small plaque (magnified in A2'/B2') showing bundled fibers that are clearly distinguishable by STED, but not by Confocal imaging. **C2** Fluorescence intensity distribution profile shows that STED could distinguish two fibers, 80 and 110 nm in diameter, that are 260 nm apart (black squares and corresponding Gaussian fit (red line)), whereas confocal imaging showed a blurred rod-like structure with a broad, single-peak fluorescence intensity distribution profile (grey diamonds and corresponding Gaussian fit (blue line)). **A3/B3** STED (**A3**) and CLSM (**B3**) images of a cell-dense area (DAPI nuclear stain (blue)), showing short fibrils in the perinuclear region and long fibrils located between cells that are hardly visible due to the large extracellular depositions of structured aggregates present nearby, where the 1C3-DyLight633 antibody binds in a large excess (red). Scale bar in all images is 2 µm

filaments, sheet-like rather than ribbon-like assemblies etc. [38]. Hence, morphological analysis of plaques nanoscale structure may better reflect underlying AD pathology.

Optimal use of antibodies and other staining in AD diagnostics is far from settled. Comparison of traditionally used methods for Aβ amyloid plaque labelling, e.g. Congo red, Gallyas silver staining and Thioflavin-S, with one of the more commonly used antibodies for immunohistochemistry [39], antibody cross-reactivity analysis [40], and inter-laboratory comparison of neuropathological assessments of Aβ [41], showed good agreement in dichotomized valuations, presence/absence of Aβ plaques, but limited agreement in any more elaborate quantification analysis. In this context, the use of super-resolution microscopy and monoclonal antibodies that selectively reacts with Aβ aggregates, including soluble oligomers and insoluble fibrils, but do not bind to the monomers present in large excess, could be of high value as it could result in histopathological diagnostics that better reflect underlying pathology. Structured Aβ amyloid fibrils rather than unstructured protein aggregates are stable to the action of denaturing agents and proteases, and they have the mechanical strength of industrial materials [42]. The ability to observe individual Aβ amyloid fibrils with high resolution and sensitivity in relation to cell structures (Fig. $3A_3$), may enable studies on how amyloid fibrils cause damage to neighbouring cells. Studies of the anatomical relationship between fibrils and cell structure are important as there is evidence that amyloid fibrils can mechanically distort adjacent cells [43].

Spread of Aβ *via* neuro-anatomical pathways may be characterized in detail. For example, Armstrong and coworkers have compared the spatial patterns of amyloid deposits in sporadic AD and Down's syndrome, finding that different disorders show considerable similarities in the spatial patterns of Aβ deposits, which may, in turn, suggest that the spread of Aβ *via* neuro-anatomical pathways may be common to several disorders [11]. However, differences were also observed among disorders. For example, the diffuse Aβ deposits were more frequently distributed in regular clusters in AD, while cluster sizes of the diffuse and primitive deposits were significantly smaller in chronic traumatic encephalopathy [11]. Results from intracerebral injection of Aβ-rich brain extracts suggest that Aβ aggregation can be initiated by seeding [44]. Interestingly, it has been found that tau misfolding can propagate between individual hippocampal neurons [45]. The STED methodology can be useful for studies of such propagation, and it will be interesting to know whether similar transfer holds for Aβ, as network patterns of Aβ deposition have been described in Parkinson's disease [46]. Astrocytes may also play a role, as there is evidence for toxic Aβ oligomers induced self-replication in astrocytes triggering neuronal injury [47, 48] developed spatially extended nucleation-aggregation-fragmentation models for the dynamics of prion-like neurodegenerative protein-spreading in the brain. The prion-like hypothesis of neurodegenerative diseases states that the accumulation of misfolded proteins in the form of aggregates is responsible for tissue death and associated neurodegenerative pathology and cognitive decline. The spreading and aggregation of both Aβ and tau molecules in the brain connectome has recently been modelled [49]. In a mouse model, a "feed-forward" mechanism whereby Aβ plaques enhance endogenous α-synuclein seeding and spreading over time post-injection has been proposed [50].

Finally, recent success in the development of immunotherapies against Aβ for the treatment of AD that were shown to reduce the amyloid load [28], underline the need for observing at the nanoscale spatial resolution local plaque clearance mechanisms while monitoring the therapeutic efficacy of these treatments. STED microscopy may also shed light on our understanding of mechanisms through which negative side effects may arise [44] and may also help us understand how amyloid deposition builds-up/is cleared within cerebral vessels in cerebral amyloid angiopathy (CAA).

Acknowledgements
We thank Dr. Jan Vávra and Dr. Janina Hanne, Abberior Instruments for the STEDYCON nanoscope demonstration and Dr. Sergej Masich 3D-EM-Facility, Department of Cellular and Molecular Biology, Karolinska Institutet, for providing the TEM image of $Aβ_{40}$ aggregates.

Author contributions
All authors contributed to the study's conception and design. Sample collection, material preparation, data collection and analysis were performed by SO, BJ, AM, LG-L, LS, EA and AT. The first draft of the manuscript was written by BJ and SO. All authors contributed to manuscript revision, and have read and approved the final version.

Funding
Open access funding provided by Karolinska Institute. Financial support from The Knut and Alice Wallenberg Foundation (KAW 2011.0218), the Swedish Research Council (2018–05337, 2022–03402), the Foundation for Strategic Research (SBE13-0115), The Olav Thon Foundation, The Olle Engkvist's Foundation (Grant 199–0480), Åhlén Foundation, Magnus Bergvall's Foundation (2020–04043, 2021–04376), UAB-GE-260408 and European Union's Horizon 2020 Research and Innovation Program (ArrestAD H2020 Fet-OPEN-1-2016-2017-737390) is gratefully acknowledged. We thank Frank M. LaFerla, Institute for Memory Impairments and Neurological Disorders, University of California, Irvine, CA, United States, for kindly providing the progenitors of the Spanish colonies of homozygous 3×Tg-AD and NTg mice. Dr. Sho Oasa is partially supported by the Strategic Research Program in Neuroscience (Strat Neuro) and Dr. Ann Tiiman by the Loo and Hans Osterman Foundation for Medical Research.

Availability of data and materials
All data and related analyses are included in this published article. All other data is available from the corresponding author upon request.

Declarations

Ethics approval and consent to participate

Experiments were performed in accordance with the relevant guidelines from the Swedish National Board for Laboratory Animals, the Spanish legislation and the European Community Council Directive (2010/63/UE) on this subject under the protocol CEEAH 3588/DMAH 9452 approved by the Ethics Committee of Departament de Medi Ambient i Habitatge, Generalitat de Catalunya on March 8, 2019.

Consent for publication

Not applicalble.

Competing interests

The authors BJ, SO, AMS, AT, LT, LGL and VV have declared that no competing interests exists. LS, EA, CM, and LL are employees and shareholders of BioArctic. LL is BioArctic co-founder and board member.

Author details

[1]Department of Clinical Neuroscience, Karolinska Institutet, SE-17176 Stockholm, Sweden. [2]Theme Aging, Karolinska University Hospital, Karolinska Institutet, SE-17176 Stockholm, Sweden. [3]Institut de Neurociències, Universitat Autònoma de Barcelona, 08193 Barcelona, Spain. [4]Department of Psychiatry and Forensic Medicine, School of Medicine, Universitat Autònoma de Barcelona, 08193 Barcelona, Spain. [5]BioArctic AB, Stockholm, Sweden.

Received: 1 May 2023 Accepted: 14 July 2023
Published online: 04 August 2023

References

1. Hardy J, Selkoe DJ. The amyloid hypothesis of Alzheimer's disease: progress and problems on the road to therapeutics. Science. 2002; 297(5580): 353-6. doi: https://doi.org/10.1126/science.1072994. Erratum in: Science. 2002; 297(5590): 2209.
2. O'Brien RJ, Wong PC. Amyloid precursor protein processing and Alzheimer's disease. Annu Rev Neurosci. 2011;34:185–204. https://doi.org/10.1146/annurev-neuro-061010-113613.
3. Hartmann T, Bieger SC, Brühl B, Tienari PJ, Ida N, Allsop D, Roberts GW, Masters CL, Dotti CG, Unsicker K, Beyreuther K. Distinct sites of intracellular production for Alzheimer's disease A beta40/42 amyloid peptides. Nat Med. 1997;3(9):1016–20. https://doi.org/10.1038/nm0997-1016.
4. D'Andrea MR, Nagele RG, Wang HY, Peterson PA, Lee DH. Evidence that neurones accumulating amyloid can undergo lysis to form amyloid plaques in Alzheimer's disease. Histopathology. 2001;38(2):120–34. https://doi.org/10.1046/j.1365-2559.2001.01082.x.
5. Mochizuki A, Tamaoka A, Shimohata A, Komatsuzaki Y, Shoji S. Abeta42-positive non-pyramidal neurons around amyloid plaques in Alzheimer's disease. Lancet. 2000; 355(9197): 42–3. https://doi.org/10.1016/S0140-6736(99)04937-5. Erratum in: Lancet. 2000; 355(9202): 502.
6. Gouras GK, Tsai J, Naslund J, Vincent B, Edgar M, Checler F, Greenfield JP, Haroutunian V, Buxbaum JD, Xu H, Greengard P, Relkin NR. Intraneuronal Abeta42 accumulation in human brain. Am J Pathol. 2000;156(1):15–20. https://doi.org/10.1016/s0002-9440(10)64700-1.
7. Lashuel HA, Labrenz SR, Woo L, Serpell LC, Kelly JW. Protofilaments, filaments, ribbons, and fibrils from peptidomimetic self-assembly: implications for amyloid fibril formation and materials science. J Am Chem Soc. 2000;122(22):5262–77. https://doi.org/10.1021/ja9937831.
8. Stromer T, Serpell LC. Structure and morphology of the Alzheimer's amyloid fibril. Microsc Res Tech. 2005;67(3–4):210–7. https://doi.org/10.1002/jemt.20190.
9. Kumar-Singh S, Pirici D, McGowan E, Serneels S, Ceuterick C, Hardy J, Duff K, Dickson D, Van Broeckhoven C. Dense-core plaques in Tg2576 and PSAPP mouse models of Alzheimer's disease are centered on vessel walls. Am J Pathol. 2005;167(2):527–43. https://doi.org/10.1016/S0002-9440(10)62995-1.
10. Rasmussen J, Mahler J, Beschorner N, Kaeser SA, Häsler LM, Baumann F, Nyström S, Portelius E, Blennow K, Lashley T, Fox NC, Sepulveda-Falla D, Glatzel M, Oblak AL, Ghetti B, Nilsson KPR, Hammarström P, Staufenbiel M, Walker LC, Jucker M. Amyloid polymorphisms constitute distinct clouds of conformational variants in different etiological subtypes of Alzheimer's disease. Proc Natl Acad Sci U S A. 2017;114(49):13018–23. https://doi.org/10.1073/pnas.1713215114.
11. Armstrong RA, Cairns NJ, Myers D, Smith CU, Lantos PL, Rossor MN. A comparison of beta-amyloid deposition in the medial temporal lobe in sporadic Alzheimer's disease, Down's syndrome and normal elderly brains. Neurodegeneration. 1996;5(1):35–41. https://doi.org/10.1006/neur.1996.0005.
12. Nordstedt C, Näslund J, Tjernberg LO, Karlström AR, Thyberg J, Terenius L. The Alzheimer a beta peptide develops protease resistance in association with its polymerization into fibrils. J Biol Chem. 1994;269(49):30773–6.
13. Sahl SJ, Hell SW. High-resolution 3D light microscopy with STED and RESOLFT. In: Bille JF, editor. High resolution imaging in microscopy and ophthalmology: new frontiers in biomedical optics. Cham (CH): Springer; 2019.
14. Vicidomini G, Bianchini P, Diaspro A. STED super-resolved microscopy. Nat Methods. 2018;15(3):173–82. https://doi.org/10.1038/nmeth.4593.
15. Mahou P, Curry N, Pinotsi D, Kaminski Schierle G, Kaminski C. Stimulated emission depletion microscopy to study amyloid fibril formation, SPIE BiOS. SPIE. 2015;9331:76-85.
16. Zhang WI, Antonios G, Rabano A, Bayer TA, Schneider A, Rizzoli SO. Super-Resolution Microscopy of Cerebrospinal Fluid biomarkers as a Tool for Alzheimer's Disease Diagnostics. J Alzheimers Dis. 2015;46(4):1007–20. https://doi.org/10.3233/JAD-150064.
17. Schedin-Weiss S, Caesar I, Winblad B, Blom H, Tjernberg LO. Super-resolution microscopy reveals γ-secretase at both sides of the neuronal synapse. Acta Neuropathol Commun. 2016;4:29. https://doi.org/10.1186/s40478-016-0296-5.
18. Yu Y, Gao Y, Winblad B, Tjernberg LO, Schedin-Weiss S. A Super-Resolved View of the Alzheimer's Disease-Related amyloidogenic pathway in hippocampal neurons. J Alzheimers Dis. 2021;83(2):833–52. https://doi.org/10.3233/JAD-215008.
19. Kedia S, Mandal K, Netrakanti PR, Jose M, Sisodia SS, Nair D. Nanoscale organization of Nicastrin, the substrate receptor of the γ-secretase complex, as independent molecular domains. Mol Brain. 2021;14(1):158. https://doi.org/10.1186/s13041-021-00855-x.
20. Viana da Silva S, Haberl MG, Zhang P, Bethge P, Lemos C, Gonçalves N, Gorlewicz A, Malezieux M, Gonçalves FQ, Grosjean N, Blanchet C, Frick A, Nägerl UV, Cunha RA, Mulle C. Early synaptic deficits in the APP/PS1 mouse model of Alzheimer's disease involve neuronal adenosine A2A receptors. Nat Commun. 2016;7:11915. https://doi.org/10.1038/ncomms11915.
21. Kubo A, Misonou H, Matsuyama M, Nomori A, Wada-Kakuda S, Takashima A, Kawata M, Murayama S, Ihara Y, Miyasaka T. Distribution of endogenous normal tau in the mouse brain. J Comp Neurol. 2019;527(5):985–98. https://doi.org/10.1002/cne.24577.
22. Querol-Vilaseca M, Colom-Cadena M, Pegueroles J, Nuñez-Llaves R, Luque-Cabecerans J, Muñoz-Llahuna L, Andilla J, Belbin O, Spires-Jones TL, Gelpi E, Clarimon J, Loza-Alvarez P, Fortea J, Lleó A. Nanoscale structure of amyloid-β plaques in Alzheimer's disease. Sci Rep. 2019;9(1):5181. https://doi.org/10.1038/s41598-019-41443-3.
23. Hernández JM, Buisson A, Wang I, Vial JC. Improved optical slicing by stimulated emission depletion light sheet microscopy. Biomed Opt Express. 2020;11(2):660–71. https://doi.org/10.1364/BOE.379646.
24. Bigi A, Ermini E, Chen SW, Cascella R, Cecchi C. Exploring the release of toxic oligomers from α-synuclein fibrils with antibodies and STED microscopy. Life (Basel). 2021;11(5):431. https://doi.org/10.3390/life11050431.
25. Torra J, Bondia P, Gutierrez-Erlandsson S, Sot B, Flors C. Long-term STED imaging of amyloid fibers with exchangeable thioflavin T. Nanoscale. 2020;12(28):15050–3. https://doi.org/10.1039/d0nr02961k.
26. Ruiz-Arias A, Jurado R, Fueyo-Gonzalez F, Herranz R, Galvez N, Gonzalez-Vera JA, Orte A, Ruiz-Arias Á, Jurado R, Fueyo-González F, Gálvez N. González-Vera, Juan A. A FRET pair for quantitative and superresolution imaging of amyloid fibril formation. Sens Actuators B. 2022;350:130882. https://doi.org/10.1016/j.snb.2021.130882.
27. Sahl SJ, Lau L, Vonk WI, Weiss LE, Frydman J, Moerner WE. Delayed emergence of subdiffraction-sized mutant huntingtin fibrils following inclusion body formation. Q Rev Biophys. 2016;49:e2. https://doi.org/10.1017/S0033583515000219.

28. van Dyck CH, Swanson CJ, Aisen P, Bateman RJ, Chen C, Gee M, Kanekiyo M, Li D, Reyderman L, Cohen S, Froelich L, Katayama S, Sabbagh M, Vellas B, Watson D, Dhadda S, Irizarry M, Kramer LD, Iwatsubo T. Lecanemab in Early Alzheimer's Disease. N Engl J Med. 2023;388(1):9–21. https://doi.org/10.1056/NEJMoa2212948.
29. Söderberg L, Johannesson M, Nygren P, Laudon H, Eriksson F, Osswald G, Möller C, Lannfelt L. Lecanemab, aducanumab, and gantenerumab - binding profiles to different forms of amyloid-beta might explain efficacy and side effects in clinical trials for Alzheimer's disease. Neurotherapeutics. 2022. https://doi.org/10.1007/s13311-022-01308-6.
30. Linse S, Scheidt T, Bernfur K, Vendruscolo M, Dobson CM, Cohen SIA, Sileikis E, Lundqvist M, Qian F, O'Malley T, Bussiere T, Weinreb PH, Xu CK, Meisl G, Devenish SRA, Knowles TPJ, Hansson O. Kinetic fingerprints differentiate the mechanisms of action of anti-Aβ antibodies. Nat Struct Mol Biol. 2020;27(12):1125–33. https://doi.org/10.1038/s41594-020-0505-6.
31. Oddo S, Caccamo A, Shepherd JD, Murphy MP, Golde TE, Kayed R, Metherate R, Mattson MP, Akbari Y, LaFerla FM. Triple-transgenic model of Alzheimer's disease with plaques and tangles: intracellular abeta and synaptic dysfunction. Neuron. 2003;39(3):409–21. https://doi.org/10.1016/s0896-6273(03)00434-3.
32. Englund H, Sehlin D, Johansson AS, Nilsson LN, Gellerfors P, Paulie S, Lannfelt L, Pettersson FE. Sensitive ELISA detection of amyloid-beta protofibrils in biological samples. J Neurochem. 2007;103(1):334–45. https://doi.org/10.1111/j.1471-4159.2007.04759.x.
33. Keller RW, Kühn U, Aragón M, Bornikova L, Wahle E, Bear DG. The nuclear poly(A) binding protein, PABP2, forms an oligomeric particle covering the length of the poly(A) tail. J Mol Biol. 2000;297(3):569–83. https://doi.org/10.1006/jmbi.2000.3572.
34. Jiménez JL, Guijarro JI, Orlova E, Zurdo J, Dobson CM, Sunde M, Saibil HR. Cryo-electron microscopy structure of an SH3 amyloid fibril and model of the molecular packing. EMBO J. 1999;18(4):815–21. https://doi.org/10.1093/emboj/18.4.815.
35. Wang J, Gülich S, Bradford C, Ramirez-Alvarado M, Regan L. A twisted four-sheeted model for an amyloid fibril. Structure. 2005;13(9):1279–88. https://doi.org/10.1016/j.str.2005.06.010.
36. Schweighauser M, Arseni D, Bacioglu M, Huang M, Lövestam S, Shi Y, Yang Y, Zhang W, Kotecha A, Garringer HJ, Vidal R, Hallinan GI, Newell KL, Tarutani A, Murayama S, Miyazaki M, Saito Y, Yoshida M, Hasegawa K, Lashley T, Revesz T, Kovacs GG, van Swieten J, Takao M, Hasegawa M, Ghetti B, Spillantini MG, Ryskeldi-Falcon B, Murzin AG, Goedert M, Scheres SHW. Age-dependent formation of TMEM106B amyloid filaments in human brains. Nature. 2022;605(7909):310–4. https://doi.org/10.1038/s41586-022-04650-z.
37. Yang Y, Arseni D, Zhang W, Huang M, Lövestam S, Schweighauser M, Kotecha A, Murzin AG, Peak-Chew SY, Macdonald J, Lavenir I, Garringer HJ, Gelpi E, Newell KL, Kovacs GG, Vidal R, Ghetti B, Ryskeldi-Falcon B, Scheres SHW, Goedert M. Cryo-EM structures of amyloid-β 42 filaments from human brains. Science. 2022;375(6577):167–72. https://doi.org/10.1126/science.abm7285.
38. Wood SJ, Maleeff B, Hart T, Wetzel R. Physical, morphological and functional differences between ph 5.8 and 7.4 aggregates of the Alzheimer's amyloid peptide Abeta. J Mol Biol. 1996;256(5):870–7. https://doi.org/10.1006/jmbi.1996.0133.
39. Shi XZ, Wei X, Sha LZ, Xu Q. Comparison of β-Amyloid plaque labeling methods: antibody staining, Gallyas Silver Staining, and Thioflavin-S staining. Chin Med Sci J. 2018;33(3):167–73. https://doi.org/10.24920/03476.
40. Hunter S, Brayne C. Do anti-amyloid beta protein antibody cross reactivities confound Alzheimer disease research? J Negat Results Biomed. 2017; 16(1): 1. doi: https://doi.org/10.1186/s12952-017-0066-3. Erratum in: J Negat Results Biomed. 2017; 16(1): 8.
41. Alafuzoff I, Pikkarainen M, Arzberger T, Thal DR, Al-Sarraj S, Bell J, Bodi I, Budka H, Capetillo-Zarate E, Ferrer I, Gelpi E, Gentleman S, Giaccone G, Kavantzas N, King A, Korkolopoulou P, Kovács GG, Meyronet D, Monoranu C, Parchi P, Patsouris E, Roggendorf W, Stadelmann C, Streichenberger N, Tagliavini F, Kretzschmar H. Inter-laboratory comparison of neuropathological assessments of beta-amyloid protein: a study of the BrainNet Europe consortium. Acta Neuropathol. 2008;115(5):533–46. https://doi.org/10.1007/s00401-008-0358-2.
42. Dovidchenko NV, Leonova EI, Galzitskaya OV. Mechanisms of amyloid fibril formation. Biochem (Mosc). 2014;79(13):1515–27. https://doi.org/10.1134/S0006297914130057.
43. Koike H, Nishi R, Ikeda S, Kawagashira Y, Iijima M, Sakurai T, Shimohata T, Katsuno M, Sobue G. The morphology of amyloid fibrils and their impact on tissue damage in hereditary transthyretin amyloidosis: an ultrastructural study. J Neurol Sci. 2018;394:99–106. https://doi.org/10.1016/j.jns.2018.09.011.
44. Friesen M, Meyer-Luehmann M. Aβ seeding as a Tool to study cerebral amyloidosis and Associated Pathology. Front Mol Neurosci. 2019;12:233. https://doi.org/10.3389/fnmol.2019.00233.
45. Hallinan GI, Vargas-Caballero M, West J, Deinhardt K. Tau misfolding efficiently propagates between individual intact hippocampal neurons. J Neurosci. 2019;39(48):9623–32. https://doi.org/10.1523/JNEUROSCI.1590-19.2019.
46. Kim HR, Lee P, Seo SW, Roh JH, Oh M, Oh JS, Oh SJ, Kim JS, Jeong Y. Comparison of amyloid β and tau spread models in Alzheimer's Disease. Cereb Cortex. 2019;29(10):4291–302. https://doi.org/10.1093/cercor/bhy311.
47. Dujardin S, Hyman BT. Tau prion-like propagation: state of the art and current challenges. Adv Exp Med Biol. 2019;1184:305–25. https://doi.org/10.1007/978-981-32-9358-8_23.
48. Wang W, Hou TT, Jia LF, Wu QQ, Quan MN, Jia JP. Toxic amyloid-β oligomers induced self-replication in astrocytes triggering neuronal injury. EBioMedicine. 2019;42:174–87. https://doi.org/10.1016/j.ebiom.2019.03.049.
49. Fornari S, Schäfer A, Kuhl E, Goriely A. Spatially-extended nucleation-aggregation-fragmentation models for the dynamics of prion-like neurodegenerative protein-spreading in the brain and its connectome. J Theor Biol. 2020;486:110102. https://doi.org/10.1016/j.jtbi.2019.110102.
50. Bassil F, Brown HJ, Pattabhiraman S, Iwasyk JE, Maghames CM, Meymand ES, Cox TO, Riddle DM, Zhang B, Trojanowski JQ, Lee VM. Amyloid-Beta (Aβ) plaques promote seeding and spreading of alpha-synuclein and tau in a mouse model of Lewy Body Disorders with Aβ Pathology. Neuron. 2020;105(2):260–275e6. https://doi.org/10.1016/j.neuron.2019.10.010.

Publisher's Note